Experiments in Fluids (2020) 61:64
https://doi.org/10.1007/s00348-020-2892-1

RESEARCH ARTICLE

Refractive index matching (RIM) using double-binary liquid–liquid mixtures

Thorben Helmers[1] · Philip Kemper[2] · Ulrich Mießner[1] · Jorg Thöming[2]

Received: 20 June 2019 / Revised: 14 January 2020 / Accepted: 17 January 2020 / Published online: 12 February 2020

Abstract

For using microscopic multiphase flows in microreactors, an exact understanding of the underlying hydrodynamic interrelations is key for successful reactor layout and reaction control. To examine the local hydrodynamic behavior, non-invasive optical measurements techniques like particle tracking velocimetry (PTV) or micro particle image velocimetry (µPIV) are the methods of choice, since they provide precise velocity measurement with excellent spatial resolution. Such optical approaches require refractive index matching (RIM) of the involved flow phases to prevent optical distortion due to light refraction and reflection at the interfaces. Established RIM approaches often provide a single degree of freedom, which is sufficient to solely match the refractive index (RI) of the flow phases. Using these approaches, the material properties (Oh number) are fixed and the relevant dimensionless numbers (Ca, Re) may only be altered hydrodynamically or geometrically. To avoid expansive geometric scaling of the microchannels, we propose an approach using two binary mixtures (double-binary mixtures) to introduce an additional degree of freedom. The approach allows examining liquid–liquid two-phase flows at a distinct velocity while being able to change the material properties (Oh number). Thus, Ca and Re can be chosen individually and the proposed RIM-approach provides undisturbed optical access. Furthermore, we present four different binary mixtures, which allow to vary the viscosity ratio of the phases. The relevant material parameters are successfully correlated to measurement data, which delivers a system of equations that determines the mass fractions and the velocities to address Re and Ca individually. A proof-of-principle for the proposed double- binary mixture RIM-approach is successfully established using µPIV raw images.

Graphic abstract

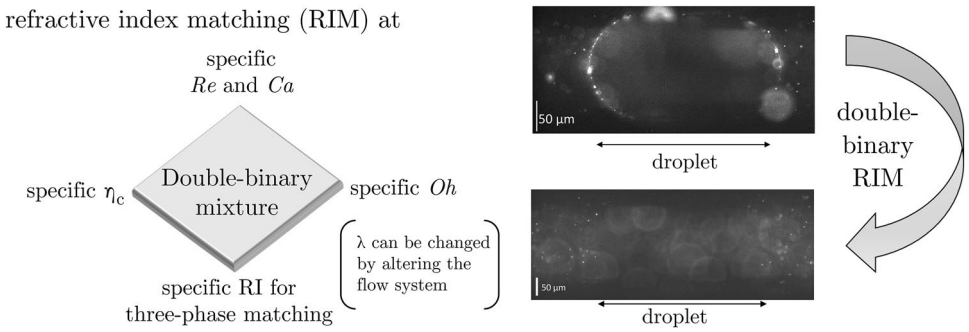

Abbreviations

µPIV	particle image velocimetry
µPTV	particle tracking velocimetry
DMSO	dimethyl sulfoxide
DOF	depth of field
NA	numerical aperture
RI	refractive index
RIM	refractive index matching

Electronic supplementary material The online version of this article (https://doi.org/10.1007/s00348-020-2892-1) contains supplementary material, which is available to authorized users.

✉ Thorben Helmers
helmers@uvt.uni-bremen.de

Extended author information available on the last page of the article

Dimensionless quantities

λ	Viscosity ratio (−)
Bo	Bond number (−)
Ca	Capillary number (−)
Mo	Morton number (−)
Oh	Ohnesorge number (−)
Re	Reynolds number (−)

Greek symbols

η	Dynamic viscosity (Pa s)
λ	Light wavelength (nm)
ρ	Density (kg m^{-3})
σ	Interfacial tension (N m^{-1})
ξ	Mass fraction (kg kg^{-1})

Roman symbols

A	Correlation factor (−)
d	Characteristic length (m)
g	Gravitational acceleration (m s^{-2})
u	Velocity (mm s^{-1})
R	Coefficient of determination (−)

Subscripts

0	Superficial
1, 2, 3	Order of correlation factor
adj	Adjusted
c	Continuous phase
d	Disperse phase
ex	Excitation
n	Nonpolar phase
p	Polar phase
s	Slug
tot	Total
tr	Tracer particle

1 Introduction and concept

Microfludic processes using liquid–liquid multiphase flows have gained great interest in the past decades (Zhao and Middelberg 2011; Chou et al. 2015; Ahmed et al. 2018; Shi et al. 2019). The applications range from chemical (Kobayashi et al. 2006; Song et al. 2006; Kralj et al. 2007; Lang et al. 2012; Tanimu et al. 2017) to biological (Clausell-Tormos et al. 2008; Mazutis et al. 2013; Chen et al. 2014; Wolf et al. 2015; Hosokawa et al. 2017) and pharmaceutical applications (Kang et al. 2014; Piao et al. 2015). The large specific surface area in combination with well-defined and allegedly easy-to-control flow structures promise a great potential for process intensification. Thus, optimal reactor design and controllability of the flow are key to raise this potential.

Deep insight into the hydrodynamic interaction of the distinct flow phases enables to tune the mass transfer rates towards more sustainable operation modes close to the optimal working point (Magnaudet and Eames 2000; Ern et al. 2012). To achieve this knowledge, numerical calculations and CFD-simulations enable parameterized studies of, e.g. liquid–liquid Taylor flows (Luis A. M. Rocha et al. 2017). Dimensionless numbers (Re, Ca) and material property ratios (Oh) can be set freely and independently to identify, e.g. critical operation modes. This allows to decrease time-consuming experimental effort to validation measurements.

The mentioned dimensionless quantities are often based on the material parameters of the continuous phase since it provides the wall contact and drives the flow of the disperse phase. The capillary number compares the viscous forces with the interfacial tension forces $\mathrm{Ca} = \frac{u_0 \eta_c}{\sigma}$ and it is based on the superficial velocity u_0, the dynamic viscosity η_c of the continuous phase and the interfacial tension σ. The Reynolds number relates the inertia forces to the viscous forces $\mathrm{Re} = \frac{\rho_c u_0 d}{\eta_c}$, where ρ_c denotes the density of the continuous phase and d the diameter of the microchannel. The Ohnesorge number $\mathrm{Oh} = \sqrt{\frac{\mathrm{Ca}}{\mathrm{Re}}}$ removes the hydrodynamic influences and solely remains as a material parameter.

For macroscopic liquid–liquid flows, the set of dimensionless variables changes with the growing influence of inertia and gravitational forces to Re, We, and the Morton number $\mathrm{Mo} = \mathrm{Bo} \cdot \mathrm{Oh}^2$, where the Weber number $\mathrm{We} = \mathrm{Ca} \cdot \mathrm{Re}$ represents the inertia forces compared to the interfacial tension forces. Mo introduces the buoyancy dependence of the flow's material system (Araújo et al. 2012) by combining the Bond number $\mathrm{Bo} = \frac{\Delta \rho g d^2}{\sigma}$ with the Ohnesorge number. Since buoyancy forces are small ($\mathrm{Bo} \ll 1$) in microfluidic applications, we base this work on the Oh number only.

Preferably non-invasive experimental methods need to be applied to investigate the hydrodynamic behavior of liquid–liquid multiphase flows supporting the numerical findings. Even in microchannels, a high spatial resolution of an entire flow field is accessible with, e.g. optical measurement techniques (Park and Kihm 2006; Kinoshita et al. 2007; Khodaparast et al. 2013). However, undistorted optical access is necessary to avoid measurement deviation due to light refraction and reflection at the experimental setup, as well as the flow phases themselves.

Often the hardware-related refraction effects of the setup can be compensated by adjusting the experimental design, e.g. avoiding curved surfaces and using corrective optics. The curved interfaces (interfacial areas) of microscopic liquid–liquid flows themselves are commonly counteracted applying refractive index matching (RIM) with one degree of freedom (Miessner et al. 2008; Ma et al. 2014; Liu et al. 2017). A broad overview of possible liquid–liquid, as well as solid–liquid refractive index matching possibilities, is given in the works of Budwig (1994) and Wright et al. (2017). Furthermore, recently

several approaches have been made using refractive index-matched systems not only to gain optical accessibility, but also to mimic special application cases like specific rheology for blood (Najjari et al. 2016; Brindise et al. 2018), high-density differences or for a buoyant jet (Clément et al. 2018; Krohn et al. 2018).

In microscopic liquid–liquid flows RIM with one degree of freedom solely allows matching the RI of one phase to the other. The material system of the phases like density, viscosity, and interfacial tension are fixed for the desired RI. The governing dimensionless numbers such as Re, Ca may only be parameterized hydrodynamically (superficial velocity) or geometrically (microchannel diameter). The monetary effort to parameterize the diameter of the microchannel is high, while the velocity alters both quantities simultaneously. Alternatively, surfactants can be added to change the interfacial tension of the material system solely, which allows to vary the ratio between Ca and Re. Since at surfactant concentrations well below the critical micelle concentration the viscosity of the host phase is not changed significantly, this approach addresses Ca only. However, the use of surfactants might introduce severe effects such as altering the hydrodynamics of the flow as well as its mass transfer properties.

In order to solve this problem, we suggest an approach using two immiscible binary mixtures to match refractive indices (Saksena et al. 2015; Cadillon et al. 2016), i.e. adding an additional degree of freedom to the system by introducing a binary mixture for each of the liquid phases. By this means, the material system becomes flexible enough to match the immiscible binary liquid mixtures optically using the entire range of RI. Hence, the simultaneous velocity-related change of Ca and Re may be compensated for by adequately adapting the material composition of the mixtures (Oh).

We carefully determine the mass fraction-dependent material properties of the involved mixtures, establish dedicated correlation functions and provide an approach to identify the necessary mass fractions of both binary mixtures and the needed superficial velocity to use this RIM system. A proof of principle is given using μPIV raw-images of two fluorescence particle-seeded microscopic Taylor flows at two Re and constant Ca at different channel heights.

Recently, the viscosity ratio of both flow phases $\lambda = \frac{\eta_d}{\eta_c}$ is reported to influence the local hydrodynamics of microscopic Taylor droplets (Rao and Wong 2018). However, the available measurements are limited to a narrow parameter range without refractive index matching (Kovalev et al. 2018; Liu et al. 2017). We suggest four combinations of well-quantified double-binary mixtures for the disperse phase as well as the continuous phase. This allows to additionally alter the viscosity ratio of the flow phases by changing the flow system.

2 Materials and methods

Within this section, the choice of the basic mixture compounds, the experimental procedures to retrieve the properties of the fluids, and the numerical approach are described. All measurements are referenced to mass fractions ξ to compensate for non-linearities in the mixing behavior.

2.1 Basic mixture compounds

For the binary mixtures of this work, we focused to mainly use nontoxic, non-hazardous, Newtonian substances. A wide range of addressable refractive indices is accomplished, when mixing substances of high and and low RI in each phase. The polar phase is chosen to be aqueous for practical reasons. The range of RI of the aqueous binary mixture is defined when using either DMSO or glycerol as Newtonian liquid to elevate the RI. The nonpolar phase is based on hexane, as it represents a tradeoff between a lower RI and hazardous properties. The nonpolar binary mixture is complemented by either anisole or sunflower-oil, which establishes a high RI range. Rheometry measurements show that in the observed range sunflower-oil also behaves Newtonian.

Combining the suggested aqueous mixtures with the nonpolar systems, the viscosity ratio λ between the phases of the flow can be changed by either inverting the flow phases or changing the combination of the materials. For that reason, we introduce and characterize different binary mixtures for the polar as well as for the non-polar phase. For low viscous mixtures with viscosity ratio below one, we suggest water/DMSO and *n*-hexane/anisole, while for high-viscosity ratio we propose to apply water/glycerol and *n*-hexane/sunflower oil. Please note that the viscosity ratio cannot be chosen freely. However, it is possible to choose a ratio below or above unity to investigate the hydrodynamic consequences.

With these mixtures, we reach a broad range of refractive indices between the pure substance's RI of *n*-hexane (RI ≈ 1.375) and glycerol/DMSO (RI ≈ 1.47). The material properties of the binary mixtures (density, viscosity, interfacial tension), as well as the refractive index, are given in Sect. 3.

2.2 Determination of material properties

The refractive indices of the used fluids were measured using a Krüss Abbe refractometer AR2008, temperated at 20 °C. The refractive indices were measured using a light wavelength of 589 nm (Sodium D1-line) with three independent measurements each. For volatile or liquids with low viscosity or low surface tension, no stable film forms between the prisms of the refractometer, which leads to a

high deviation. For this reason, the refractive indices of the *n*-hexane/anisole system for high mass fractions of anisole could not be acquired reliably. Instead, literature data are used in this case.

The interfacial tension of the double-binary mixtures was measured using a Lauda TVT drop tensiometer with a syringe of 2.5 ml and a stainless steel capillary at a temperature of 20 °C. The interfacial tensions were acquired using the volume drop method (the interfacial tension is measured based on the balance of buoyancy and surface tension of a detaching droplet). The dispersed droplet was detected with a light barrier and the interfacial tension was calculated from the droplet volume. The interfacial tension is a time-dependent property for non-pure or mixed systems. Thus, droplets with differently aged interfacial area were formed such that the interfacial tension for infinite time σ_{inf} can be derived (Wilkinson 1972; Sinzato et al. 2017). Within our work, the droplet formation times and, therefore, the surface age range between 2.5 and 60 s.

The light barrier, which detects the detachment of the ascending droplets, cannot work properly when the refractive indices are matched. Thus, we deliberately detune the mass fraction of the nonpolar phase such that a sufficient detection difference exists between the refractive indices of both phases (Δ RI = 0.01). The droplet detachment, as well as the interfacial tension, is determined at these detuned fluid compositions. The actual interfacial tension for the matched case is then retrieved by linear interpolation using the lever rule. The linear interpolation is considered valid since only the mass fraction of one of both phases is varied and the change in the mass fraction is kept small.

The measurements of the viscosities of the volatile compounds (*n*-hexane/anisole) were performed using a Malvern Kinexus Ultra Plus with solvent trap, cone-plate setup, 1° opening angle, and a stationary shear rate table 10–100 s^{-1} with 5 % stationarity tolerance. The remaining measurements were performed using a Bohlin Rheometer CS and a 30 ml double-gap system. All measurements were performed at 20 °C.

The densities of the mixtures are retrieved from literature data except for the mixture water/glycerol.

2.3 Mass-fraction and superficial velocity identification approach

Keeping in mind the definition of Re and Ca, refractive index matching at these properties is a minimization problem with the superficial velocity u_0 as the objective value. The mass fractions of the continuous phase ξ_{c} and disperse phase ξ_{d} are the control variable, which influences the material properties.

If the fluid properties of the pure substances as well as of the mixtures are known, Ca and Re can be calculated. The equations can be changed such that the superficial velocity u_0 for both numbers is a function of the continuous phase mass fraction ξ_{c}:

$$u_{0,\mathrm{Re}} = \frac{\mathrm{Re} \cdot \eta_c(\xi_{\mathrm{c}})}{\rho_{\mathrm{c}}(\xi_{\mathrm{c}}) \cdot d} \tag{1}$$

$$u_{0,\mathrm{Ca}} = \frac{\mathrm{Ca} \cdot \sigma(\xi_{\mathrm{c}})}{\eta_{\mathrm{c}}(\xi_{\mathrm{c}})} \tag{2}$$

For a minimum residuum of this optimization ($u_{0,\mathrm{Re}} = u_{0,\mathrm{Ca}}$), the correct u_0 is known as well as the corresponding mass fraction of the continuous phase ξ_{c}. The mass fraction of the disperse phase ξ_{d} can be calculated via the refractive index of the continuous phase. A working example is given in the supplementary resources.

3 Experimental results

Within this section, the material properties of the binary and RI-matched double-binary mixtures are experimentally investigated.

3.1 Properties of binary mixtures

To successfully determine the correct mass fractions of both binary mixtures and the superficial velocity, the used algorithm needs a steady optimization function to work with. However, the measurement data consist of discrete points including measurement errors. Thus, a transition of the discrete data sampling to continuous functions is necessary. As established in our last work (Helmers et al. 2019), we correlate the data with polynomial approaches for simplicity.

The equation for a polynomial function follows:

$$y = A_4 \cdot \xi^4 + A_3 \cdot \xi^3 + A_2 \cdot \xi^2 + A_1 \cdot \xi + A_0, \tag{3}$$

where y is the desired property (e.g., density, viscosity or interfacial tension), ξ the mass fraction of the mixture, and A_4–A_0 fitting coefficients for the polynomial. The polynomial coefficients for the different material properties as well as the experimental data and the range of validity are shown in the following:

At first, the densities of the binary mixtures are investigated in Fig. 1a for the polar and in Fig. 1b for the nonpolar media. The system water/glycerol shows a nearly linear behavior, while the system water/DMSO shows a peak at approximately $\xi = 0.8$. This is caused by nonlinear mixing behavior due to the similarity of water/DMSO and also effects the viscosity. The system *n*-hexane/anisole shows a nearly linear behavior, while *n*-hexane/sunflower oil shows a deviation from linearity. The correlations

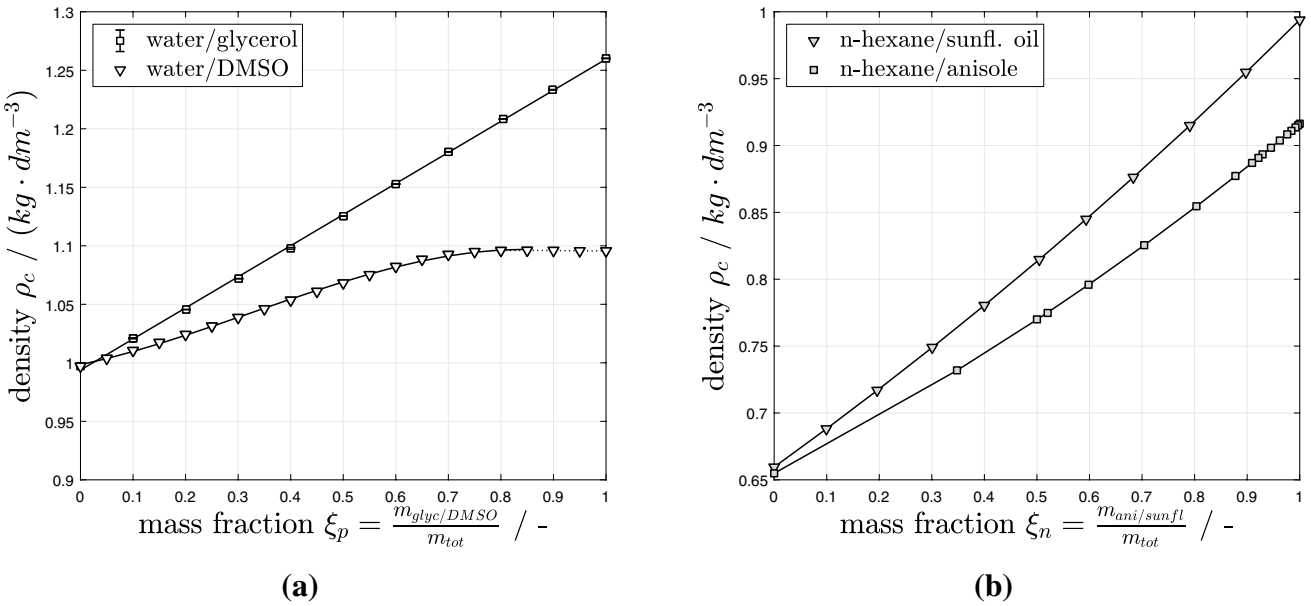

Fig. 1 Densities for the binary fluid mixtures of each phase, **a** polar phase for the system water/glycerol (literature data from (LeBel and Goring 1962)), **b** non-polar phase for the system *n*-hexane/anisole (literature data from (González et al. 1996))

Table 1 Correlation coefficients for the densities of the binary mixtures in kg cm^{-3}

Mixture	Range	A_3	A_2	A_1	A_0	R^2_{adj}
Water/glycerol	$0.00 < \xi_p < 1.00$	0	0	0.2657	0.9938	0.9997
Water/DMSO	$0.00 < \xi_p < 0.85$	− 0.1935	0.1883	0.0958	0.9984	0.9992
	$0.85 < \xi_p < 1.00$	0.2667	− 0.7371	0.6742	0.8919	0.9514
Hexan/anisole	$0.00 < \xi_n < 1.00$	0	0.129	0.2021	0.661	0.9995
Hexan/sunflower oil	$0.00 < \xi_n < 1.00$	0.0081	0.0507	0.2025	0.6549	0.9995

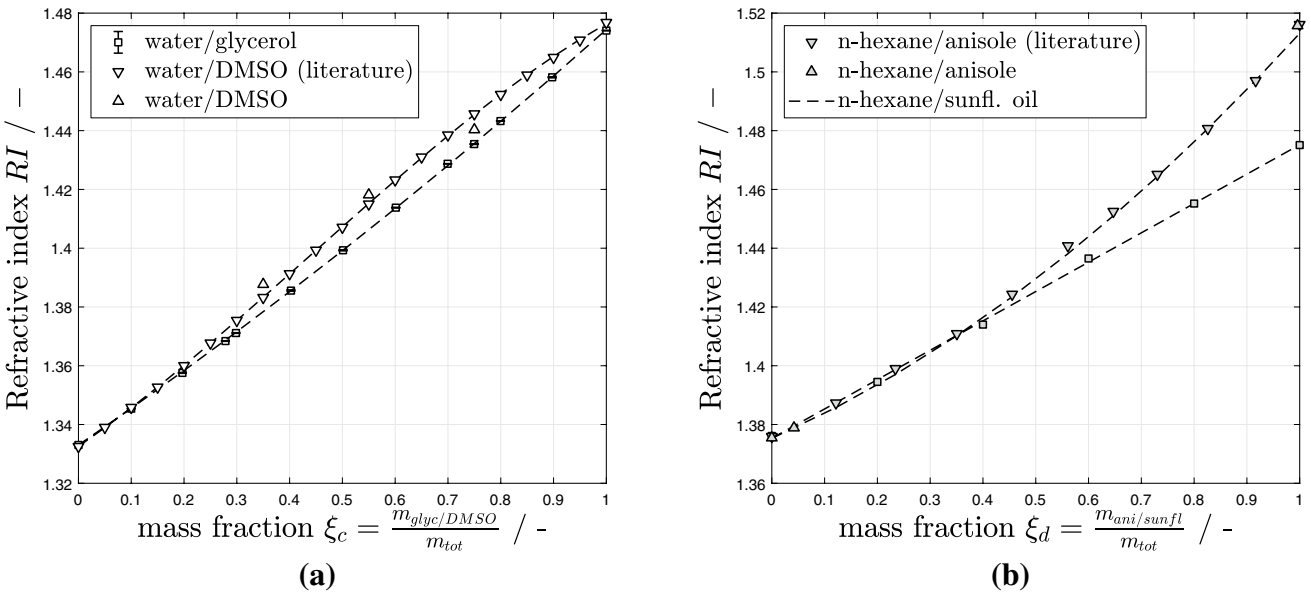

Fig. 2 Refractive indices for the fluid mixtures, **a** polar phase for the system water/glycerol and water/DMSO (literature data from (LeBel and Goring 1962)), **b** non-polar phase for the system *n*-hexane/anisole (literature data from (Al-Jimaz et al. 2005)) and *n*-hexane/sunflower oil

Table 2 Correlation coefficients for refractive index of the binary mixtures

Mixture	A_3	A_2	A_1	A_0	R^2_{adj}
Water/glycerol	0	0.0182	0.1232	1.3300	0.9997
Water/DMSO	− 0.0631	0.0834	0.1235	1.3300	0.9999
Hexan/anisole	0	0.0588	0.0790	1.3753	0.9994
Hexan/sunflower oil	0	0	0.0999	1.3753	0.9992

extracted from the measurement and literature data are shown in Table 1 together with the resulting adjusted coefficient of determination R^2_{adj}.

In Fig. 2 the refractive index of the water/glycerol mixture features a linear behavior (empty squares), while water/DMSO shows a nonlinearity for higher DMSO mass fractions (Fig. 2a, triangles). For the nonpolar substances the system *n*-hexane/sunflower-oil (filled squares) behaves nearly linear, while *n*-hexane/anisole (filled triangles) increases the slope indicating non-linear dependence

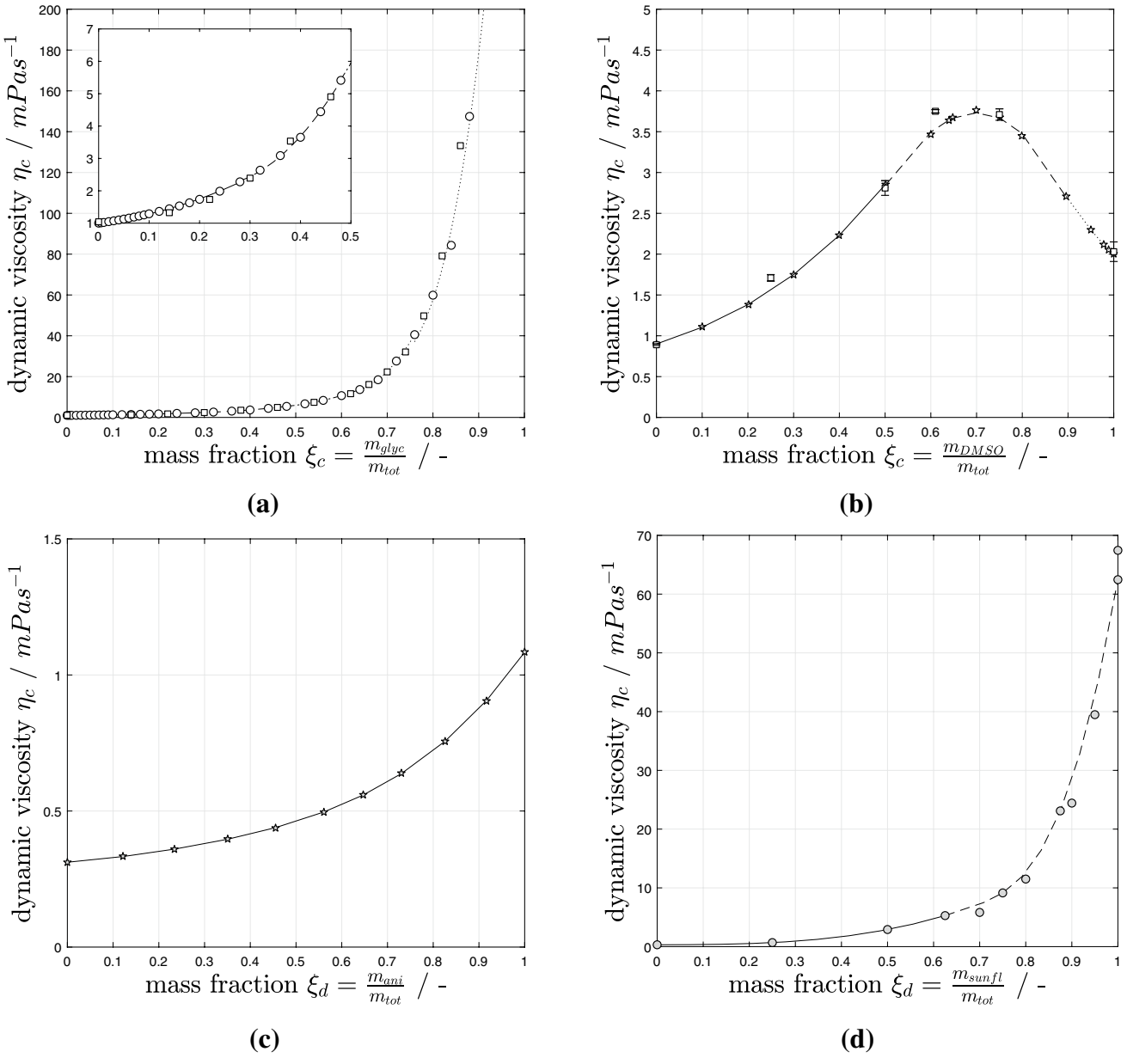

Fig. 3 Viscosities for the fluid mixtures at 20 °C, **a** polar phase water/glycerol (empty circles, Weast (1989), empty squares own measurements), **b** polar phase water/DMSO (empty stars, LeBel and Goring (1962), empty squares own measurements), **c** non-polar phase *n*-hexane/anisole (filled stars, Al-Jimaz et al. (2005)), **d** non-polar phase *n*-hexane/sunflower oil (filled circles, own measurements)

Table 3 Correlation coefficients for viscosity of the binary mixtures in mPa s

Mixture	Range	A_4	A_3	A_2	A_1	A_0	R^2_{adj}
Water/glyc.	$0.00 < \xi_p < 0.28$	0	0	9.6514	1.7769	1.0095	0.8995
	$0.28 < \xi_p < 0.48$	0	0	49.223	− 21.944	4.5865	0.9907
	$0.48 < \xi_p < 0.64$	0	0	182.8	− 153.48	36.991	0.9616
	$0.64 < \xi_p < 0.76$	0	0	1272.7	− 1557.1	488.84	0.9894
	$0.76 < \xi_p < 1.00$	0	10863.4	− 21776.31	14652.78	− 3289.78	0.9882
Water/DMSO	$0.00 < \xi_p < 0.50$	0	3.6080	2.4412	1.7748	0.8995	0.9999
	$0.50 < \xi_p < 0.89$	0	− 11.9506	0.4866	16.9060	− 4.2424	0.9950
	$0.89 < \xi_p < 1.00$	0	130.6611	− 355.8453	315.2710	− 88.0846	0.9999
Hexan/anisole	$0.00 < \xi_n < 1.00$	0.7284	− 0.4838	0.3969	0.1302	0.3117	0.9999
Hexan/sunfl. oil	$0.00 < \xi_n < 0.63$	0	19.1488	0.4864	0.1616	0.3140	0.9904
	$0.63 < \xi_n < 1.00$	0	1309.0133	− 2622.0800	1774.9866	− 399.4200	0.9848

(Fig. 2b). For all mixtures, the measurements confirm the available literature data. The correlation coefficients are shown in Table 2.

The viscosities of the four binary mixtures are given in Fig. 3. Both of the highly viscous mixtures (water/glycerol Fig. 3a, and hexane/sunflower-oil Fig. 3d) exhibit similar behavior. As intended, with a higher mass fraction of the more viscous substances, the viscosity rises. The less viscous mixtures water/DMSO (Fig. 3b) and *n*-hexane/anisole (Fig. 3c) show different behavior. While the viscosity of *n*-hexane/anisole mixtures increases quadratically with a rising mass fraction of anisole, the viscosity of water/DMSO reaches a peak at $\xi = 0.70$. For *n*-hexane/anisole no own measurements could be performed, since the high evaporation rate of the volatile hexane/anisole mixture leads to a significant deviation in the mass fraction of the mixture during the measurement. Instead, literature data are used. The correlation coefficients are shown in Table 3.

3.2 Properties of RI-matched double-binary mixtures

Since the double-binary system consists of four substances, the interfacial tension is influenced independently and possibly nonlinearly by the mass fractions of both binary mixtures. Thus, the interrelations are linearized to obtain a manageable experimental effort for the required measurements: For the use in RI-matched measurements, only the mass fractions of the matched solution need to be observed. As it is visible in Fig. 4 this simplifies the problem to a two-dimensional problem.

To retrieve the specific mass fractions of both phases for the matched case, the correlations for the RI of both phases are equated and a fit function is numerically retrieved. The behavior of the RI-matched double-binary systems is a combination of the binary mixtures. The results are shown for all double-binary mixture systems in Fig. 4.

The system water/DMSO–hexane/anisole (Fig. 4c) shows the most prominent nonlinear behavior. This is caused by the larger increase of the RI of anisole for elevated anisole mass fractions and the nonlinearity of water/DMSO. For the system water/glycerol–*n*-hexane/anisole (Fig. 4a) this behavior is as not prominent since the binary mixture water/glycerol in contrast to water/DMSO is nearly linear. As expected from the binary mixture's behavior, this also holds for the system water/glycerol–hexane/sunflower-oil (Fig. 4b), while again caused by water/DMSO, for water/DMSO–*n*-hexane/sunflower-oil nonlinearities are present at higher DMSO mass fractions (Fig. 4d). The correlation coefficients for the matched systems are shown in Table 4.

Every matched system consists of two binary mixtures with exactly one RI for the matched case and one specific mass fraction and viscosity for the polar as well as the disperse phase. Changing the mass fraction of one phase, the mass fraction of the other phase needs to be adjusted to keep the RI matching. This changes the viscosity ratio, as it also depends on the ratio of the binary mixtures of each phase. The viscosities of polar continuous phase of the high viscous systems are shown in Fig. 5. The combinations with water/glycerol show a broad range of available continuous phase viscosities.

Considering the viscosities of both flow phases, the viscosity ratio λ of the respective RI-matched material systems can be calculated. The results are shown in Fig. 6 separated for polar and nonpolar continuous phase.

In addition to the determination of the material properties that depend only on the binary mixtures themselves, the interfacial tension depends on the forces of the energetic state of the interfacial area. Thus, the determination for a quaternary fluid system is complex. For the following measurements, only the interfacial tension of the RI-matched case is of interest. Thus, we only determine values at the mass fractions of the RI-matched interfacial tensions to minimize the experimental effort. The measurement data, as well as the derived correlations, are shown in Fig. 7.

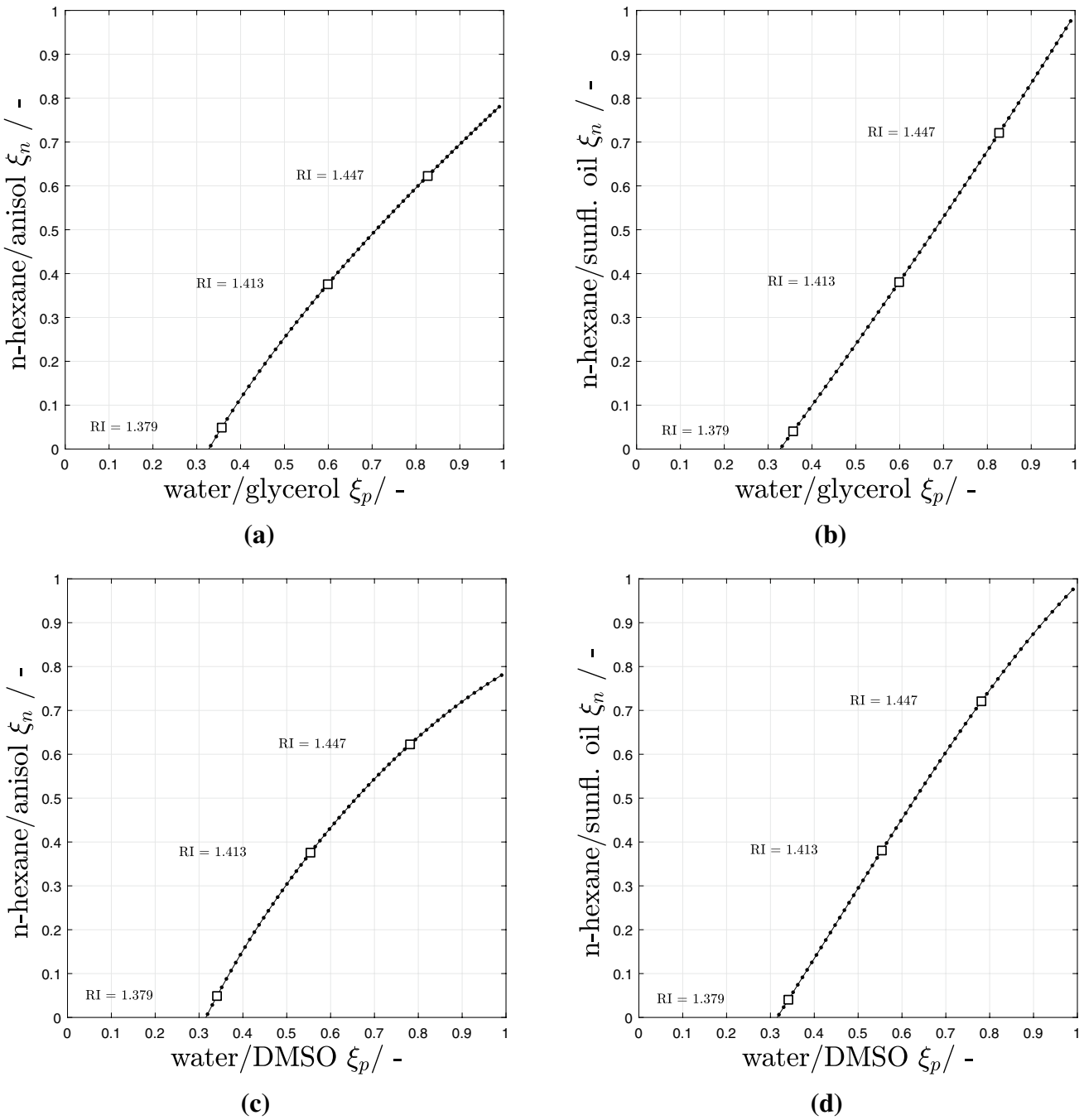

Fig. 4 Mass fractions of RI-matched double-binary mixtures with matched RI along the graph. **a** Water/glycerol–*n*-hexane/anisole, **b** water/glycerol–*n*-hexane/sunflower-oil, **c** water/DMSO–*n*-hexane/anisole, **d** water/DMSO–*n*-hexane/sunflower-oil. Large squares represent a ΔRI = 0.068 step, small dots the interiorly intermediate steps ΔRI = 0.0034

Table 4 Correlation coefficients for the mass fractions of RI-matched double-binary mixtures (range of validity for all correlations: $0.32 < \xi_p < 1$)

Mixture	A_4	A_3	A_2	A_1	A_0	R^2_{adj}
wt./glycerol–hex./anisole	− 3.5055	9.5361	− 9.8090	5.6443	− 1.0874	0.9997
wt./glycerol–hex./sunfl. oil	0	0	0.182	1.233	− 0.423	0.9999
wt./DMSO–hex./anisole	− 3.623	9.629	− 10.027	5.908	− 1.098	0.9921
wt./DMSO–hex./sunfl. oil	0	− 0.631	0.835	1.236	− 0.453	0.9999

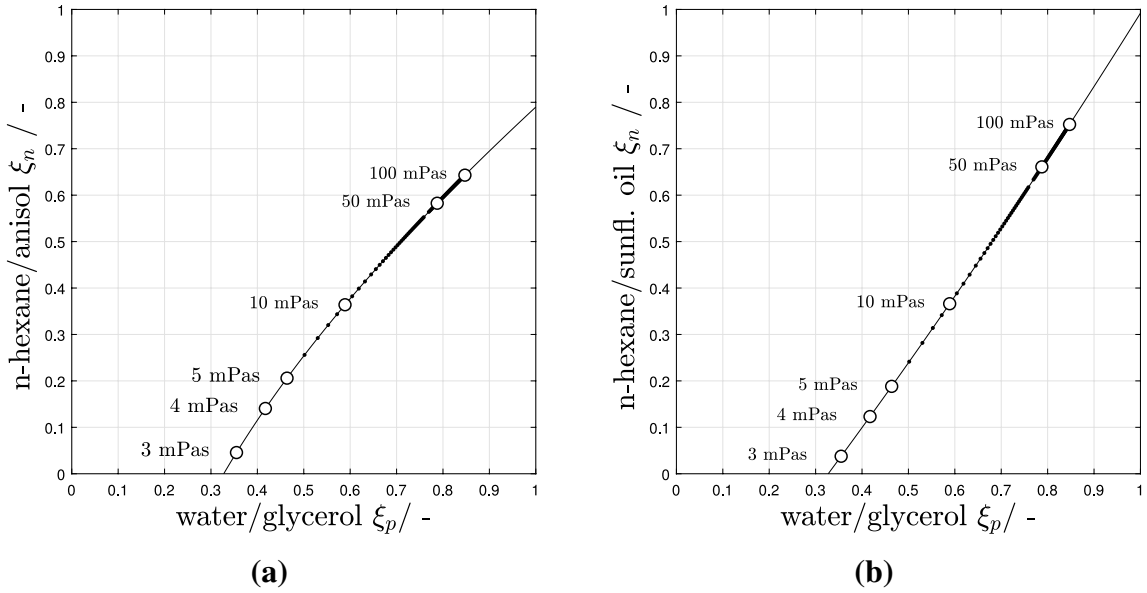

Fig. 5 Polar continuous phase viscosity η_p along the mass fractions for matched mixtures. **a** Water/glycerol–*n*-hexane/anisole, **b** water/glycerol–*n*-hexane/sunflower-oil. Large circles represent a logarithmic scale, small dots the interiorly intermediate steps. Low viscous continuous phase systems are not shown since the continuous viscosity does not change significantly over the RI-matched mass regions

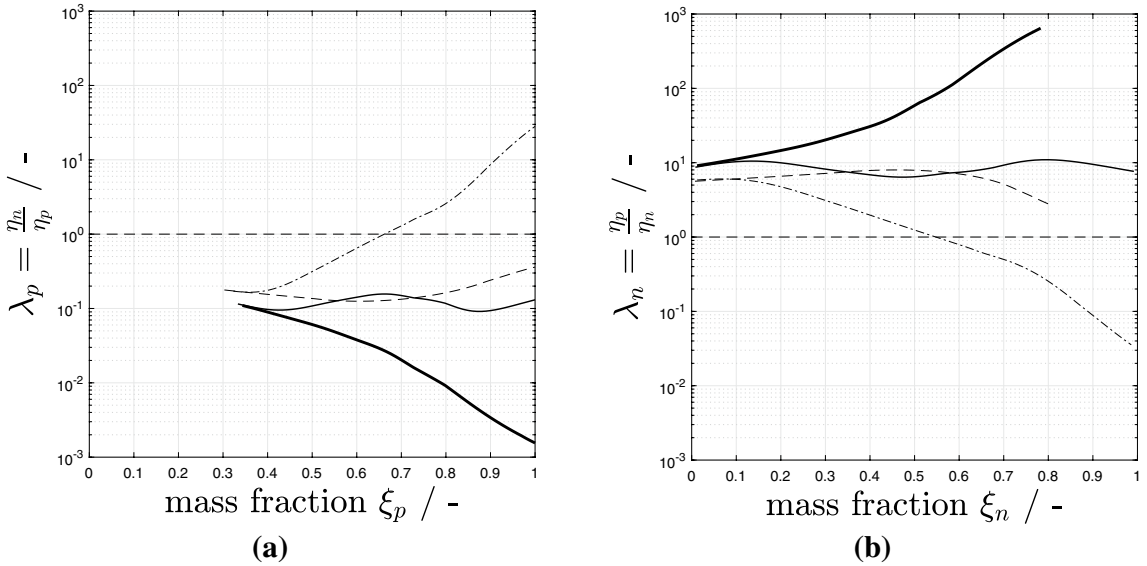

Fig. 6 Viscosity ratios λ_n and λ_p for the different systems. System water/glycerol–*n*-hexane/anisole (bold solid line), system water/glycerol–*n*-hexane/sunflower-oil (thin solid line), system water/DMSO–*n*-hexane/anisole (dashed line), system water/DMSO–*n*-hexane/sunflower-oil (dash-dotted line). **a** Continuous phase: polar, **b** continuous phase: nonpolar

The interfacial tension between the RI-matched liquids exhibits different behavior for each system. The system water/glycerol–hexane/anisole (Fig. 7a) shows an unpredictable interfacial tension development for rising mass fractions of glycerol or anisole. The interpolated values of the single measurements deviate around the correlation function. This is a sign for strong nonlinear interrelations between the four substances. Probably caused by weaker intermolecular forces between glycerol and anisole depending on the composition of the mixture. The system water/glycerol–hexane/sunflower-oil shows a minimum for equivalent fractions of all four substances ($\xi_p \approx 0.5$, $\xi_n \approx 0.5$), while the interfacial tension increases for higher amounts of glycerol or sunflower oil (Fig. 7b). As the R^2_{adj} implies, the interfacial tension of this system is weakly

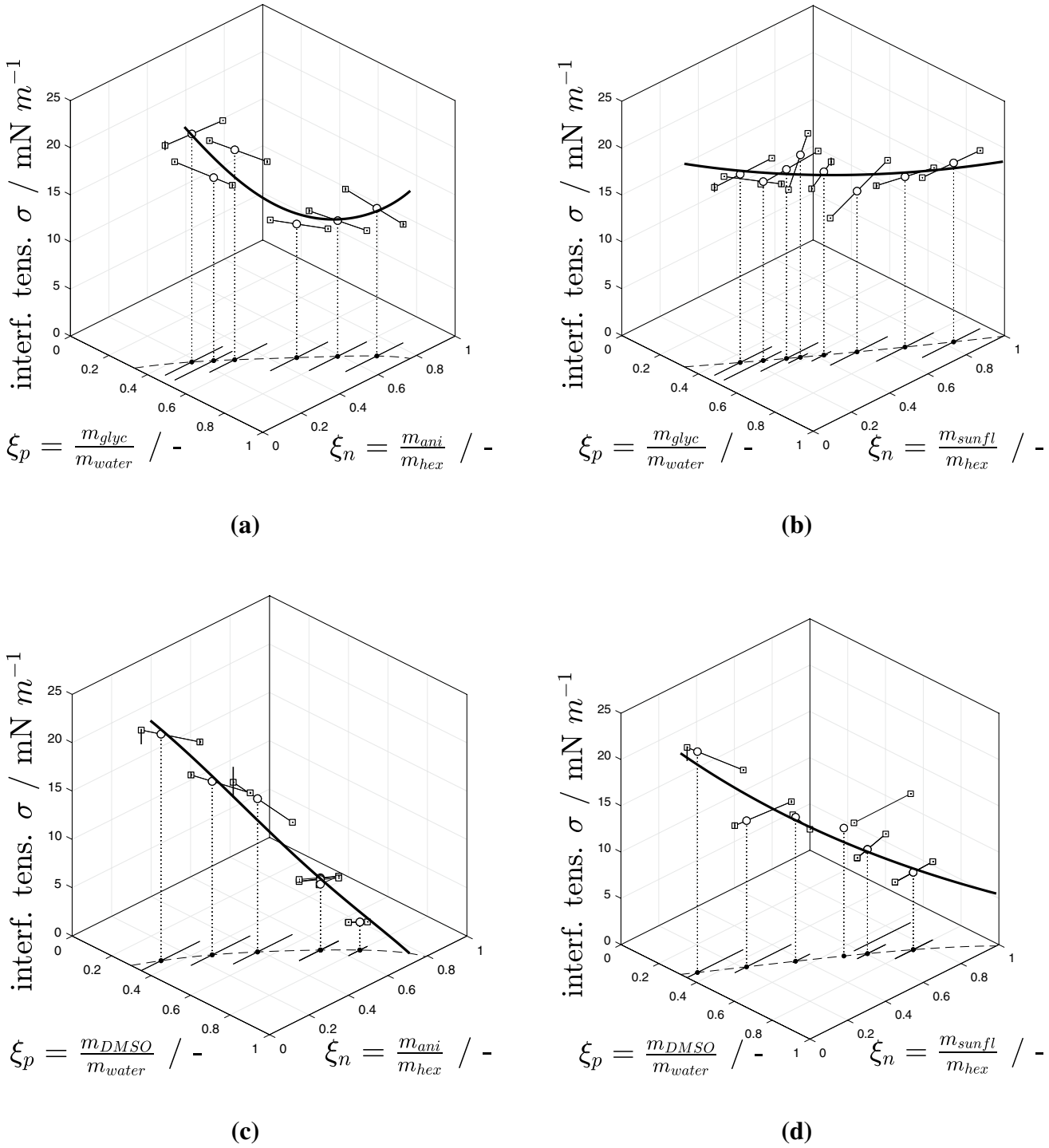

Fig. 7 Interfacial tension σ for the different systems. **a** Water/glycerol–*n*-hexane/anisole, **b** water/glycerol–*n*-hexane/sunflower-oil, **c** water/DMSO–*n*-hexane/anisole, **d** water/DMSO–*n*-hexane/sunflower-oil. Actual measurements (squares) are used to interpolate (bars) the interfacial tension at the matched phase composition (circles). The correlation for the matched interfacial tension is the correlated (bold line). Each measurement consists of five droplet formation cycles at different droplet formation times. Within each cycle, at least five droplets are formed to ensure reproducibility. Measurements are performed at slightly detuned refractive indices (see Sect. 2.2)

correlated to the mass-fractions of the flow phases. Nevertheless, the correlation is sufficient to apply the proposed RIM-approach with sufficient accuracy.

The systems involving water/DMSO expose a decreasing interfacial tension with decreasing mass-fraction of *n*-hexane. Especially the water/DMSO–hexane/anisole shows a

Table 5 Correlations coefficients for interfacial tension (range of validity $0.32 < \xi_p < 1.00$)

Mixture	A_2	A_1	A_0	R^2_{adj}
wt./glycerol - hex./anisole	79.194	−126.251	64.859	0.8090
wt./glycerol - hex./sunfl. oil	9.788	−17.484	26.340	0.1438
wt./DMSO - hex./anisole	28.231	−76.859	47.359	0.9775
wt./DMSO - hex./sunfl. oil	22.845	−56.683	39.498	0.9158

very low interfacial tension for lower mass fractions of hexane (Fig. 7c), which is caused by a diminished structural difference to hexane. Water/DMSO–*n*-hexane/sunflower-oil shows a similar decrease of the interfacial tension (Fig. 7d).

The most significant deviations (Fig. 7a, b) are situated in a range of 2 mPas. These deviations between the correlation and the interpolated data of single measurements can be caused by either the linearization or confined effects at distinct mass fractions as well as measurement errors. Since the results of the single measurements are based on at least 20 independent droplets, we consider possible measurement errors to attribute from diminutive contaminations of the volume tensiometer. The correlation coefficients for the interfacial tension for all four systems are shown in Table 5. To take care of the non-ideal behavior, we introduce a second-order polynomial fit to cover the parabolic behavior (see "Appendix").

4 Results and discussion

In this section, we discuss the experimentally determined material properties of the double-binary mixtures and deliver a proof-of-principle for the double-binary approach.

4.1 Features and limits of the double-binary approach

Based on the conducted measurements and literature data, the proposed double-binary mixture systems are described by means of correlation functions with sufficiently high accuracy. This allows to calculate the relevant dimensionless quantities Ca and Re for all accessible mass fractions and superficial velocities. This is done via the MATLAB program, which we supply with the supplementary material. Alternatively, the mass fraction and the superficial velocity can be retrieved graphically from the nomograms presented in the Appendix (Figs. 10, 11). Regarding liquid–solid refractive index matching, RI up to 1.4714 for the system water/glycerol and 1.4738 water/DMSO can be achieved. This allows to match two phase flows to the reactor material PDMS. The microreactor's cover-glass is usually aligned orthogonally to the flow and, therefore, does not need refractive index matching since on orthogonal surfaces no distortions occur. However, fused silica could still be matched.

4.2 Proof of principle

The practicability of the proposed approach for optical measurements and especially the possibility to reach the desired Re and Ca independently at a matched refractive index is proven in an experimental approach. A microscopic Taylor flow is established and optical measurements are performed in the symmetry plane (channel center plane), the channel top wall, and at an intermediate plane at 0.75 of the channel height at two different Re numbers while Ca is held constant (Fig. 8a). The experimental setup to record the PIV raw-images is described in the Appendix. In the symmetry plane at the half channel height, distortions can be quantified that arise from non-ideal refractive index matching and accumulate (Fig. 8b). In this setup, the tracer particle position in proximity of the interfacial area cannot be determined reliably, leading to a decrease of measurement precision.

Utilizing the proposed RIM-approach, the required mass fraction of the binary mixtures for the continuous and disperse phase and the superficial velocity are determined minimizing the difference of Eqs. 1, 2 as described in Sect. 2.3. Subsequently, the microscopic Taylor flow is reestablished using the calculated parameters. In the µPIV raw images, the droplet interface is not visible and optical distortions caused by the interfacial area do not occur (Fig. 8c, d). The apparent reduction of droplet length is caused by the curved droplet cap shape when the focal plane is moved towards the channel top wall. Only the tracer particles in the focal plane contribute to the image. Interfacial reflections from out of focus regions are note visible. Thus, the correlations for the refractive index as well as the solver algorithm work well.

5 Conclusion

In this study, we present and successfully validate a novel approach using double-binary mixtures for both immiscible flow phases to establish refractive index-matched microscopic multiphase flows. In comparison to classical mono-binary mixture approaches, Re and Ca can be addressed individually in a material restricted parameter set, since viscosity and interfacial tension (and thus the different flow forces) do not change in the same order of magnitude if the mass fractions of the phases' binary mixtures are varied. Alternatively, multiphase flows at different Oh at a fixed RI can be established to match the reactor material (e.g. simulating three-phase flows via monolith). We introduce two binary mixtures for a polar and nonpolar phase to enable the investigation of, e.g., different viscosity ratios λ or flow

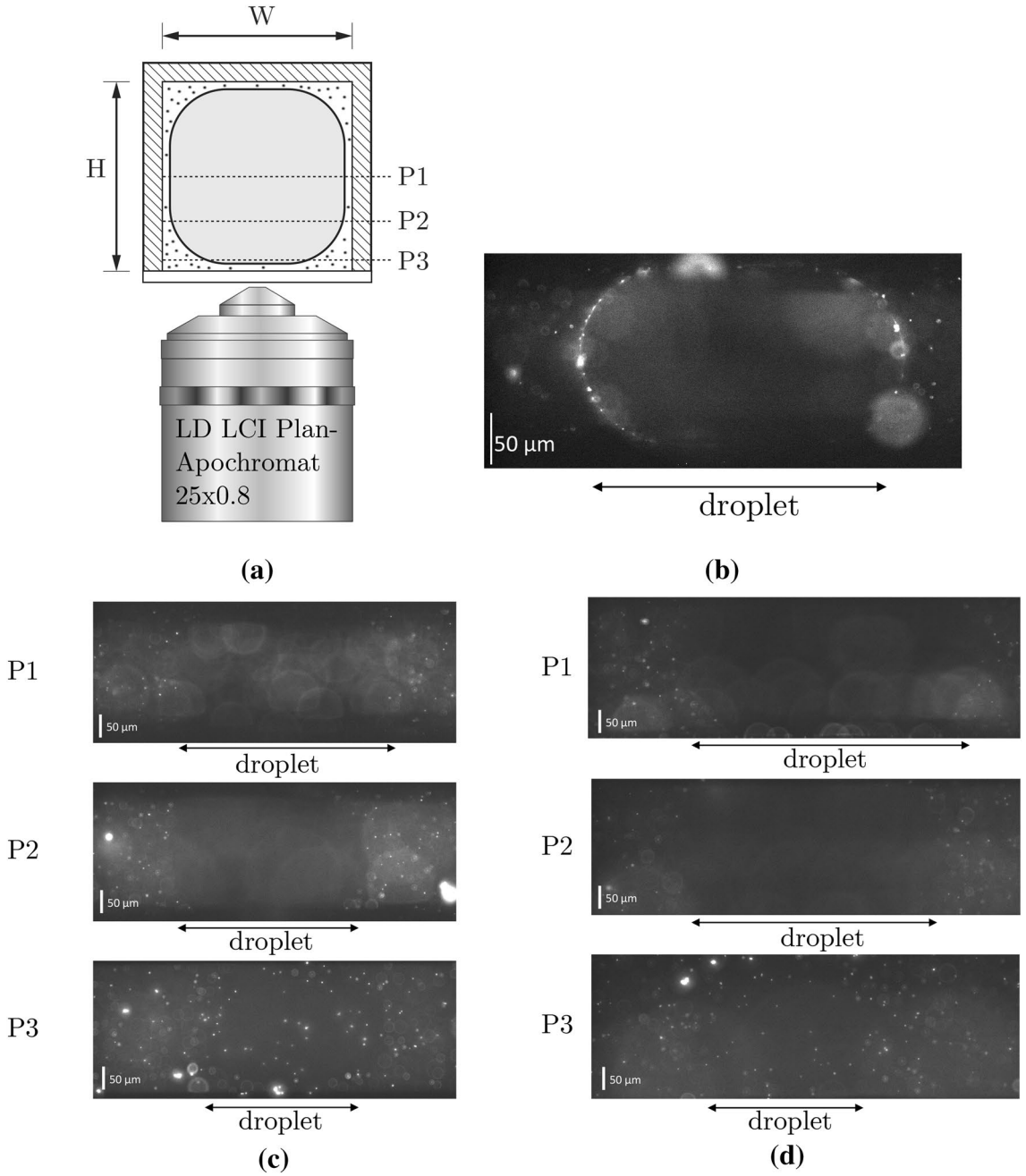

Fig. 8 Proof of principle of the proposed approach. **a** Cross-section of the microchannel with the measurement planes. **b** PIV raw-image of a particle-seeded Taylor-flow without using the proposed RIM-approach. **c**, **d** Exemplary images at two different Re and steady Ca. Water/glycerol is used as the continuous phase and seeded with fluorescent polystyrene particles, *n*-hexane/sunflower-oil as the disperse phase. Within all measurements no interfacial area is distinguishable, and no reflection or distortions of the particles are apparent. **c** Ca = 0.005, Re = 2.14, RI = 1.3838 $\xi_p = 0.391$ $\xi_n = 0.101$, **d** Ca = 0.005, Re = 0.93, RI = 1.3958 $\xi_p = 0.476$ $\xi_n = 0.221$

systems with simultaneously high or low viscosities are possible too.

Measurements for the relevant material properties (densities, viscosities, refractive index) of the binary mixtures as well as the RI-matched compositions (interfacial tensions) are carried out and compared to literature data to characterize the system. The task to establish multiphase flows at specific Re and Ca independently is identified as an optimization problem. For that purpose the material properties as well as the interfacial tension are successfully described with correlations that allow the use of a solver algorithm.

In first measurements, the capability to establish refractive index-matched Taylor flows at freely chosen Ca and Re is proven. This proof of principle is successfully conducted

using recorded µPIV raw images. With the proposed double-binary RIM-approach the specific influences on the local velocity of droplets can now be independently examined via optical flow visualization techniques (PTV, PIV).

Acknowledgements Open Access funding provided by Projekt DEAL. The contribution of P. Kemper has been supported by the German Research Foundation (DFG), Priority Program: "Reactive Bubbly Flows", SPP1740 under Grant TH 893/17-2. The authors gratefully acknowledge the financial support.

Appendix

Experimental setup of proof of principle

The experimental design follows Fig. 9: A Si-microchannel (manufactured by IMSAS Bremen) with 198 µm nearly rectangular cross-sectional area is located on a Zeiss LSM-210 inverted microscope with a motorized nosepiece and two-axis stage for precision movement. The microscope is controlled via a self-written LabView program using serial port communication.

The microscope is equipped with a Zeiss LD LCI Plan Apochromat 25x/0.8 objective to provide a high spatial resolution at a small depth of field (DOF = 1.034 µm) to receive a high resolution in the z-direction. A pulsed Nd:YAG laser (*New Wave Research Solo-PIV III*) with a 15 Hz repetition rate, 50 mJ pulse intensity, and a pulse length of 3 to 5 ns with frequency doubling (wavelength: λ_{ex} = 532 nm) serves as a light source for the measurement. Images of the flow are acquired using an active-cooled high quantum-efficient *PCO.sensicam qe 670 LD 3078* double CCD-camera with an acquisition rate of 4 Hz at a resolution of 1376 px × 1040 px. The continuous phase is seeded with particles of 1.61 µm particles. The particles are coated with FluoRed as fluorescence dye (excitation peak 530 nm, emission peak 607 nm) and are dispersed in the water/glycerol phase using an ultrasonic bath for 15 min at 20 °C.

Two syringe pumps (*Dolomite Mitos Duo XS*) supply a steady flow such that the volume flow of both phases can be individually controlled. The excitation light from the pulsed Nd:YAG laser is guided into the *Zeiss LSM210* microscope and the laser is widened with a convex lens of short focal length. The illumination is additionally averaged with a holographic diffuser.

A dichroic mirror separates the green excitation light from the red fluorescence light and directs it to the camera. To further improve the cutoff, an additional long-pass filter is mounted in the light-path to shield the camera from laser light (Fig. 9). A timing unit synchronizes the laser and the camera.

An overview of the experimental and optical parameters is given in Table 6.

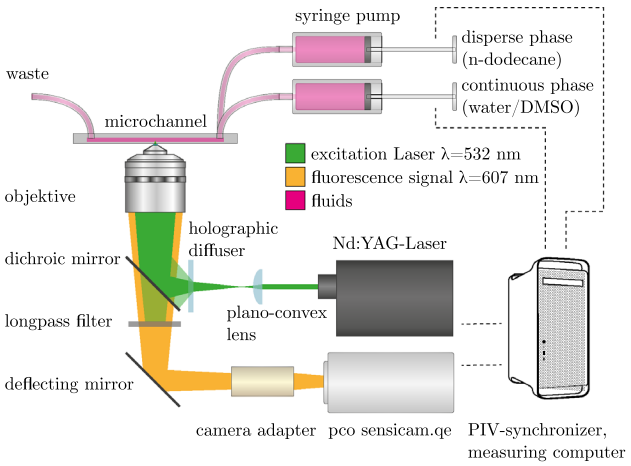

Fig. 9 Proof of principle of the double-binary mixture approach. Scheme of the experimental design for µPIV experiments

Table 6 Experimental and optical parameters of the experimental design

Property	Value	Unit
Channel width W	198	µm
Channel height H	192	µm
Excitation wavelength λ_{ex}	532	nm
Tracer particle diameter d_{tr}	1.6	µm
Tracer particle CV	2.3	%
Objective magnification	25	–
Objective NA	0.8	–
Objective DOF	0.859	µm
Particle excitation wavelength peak	530	nm
Particle emission wavelength peak	607	nm
Dichroitic mirror cutoff	552	nm
Longpass filter cutoff	550	nm

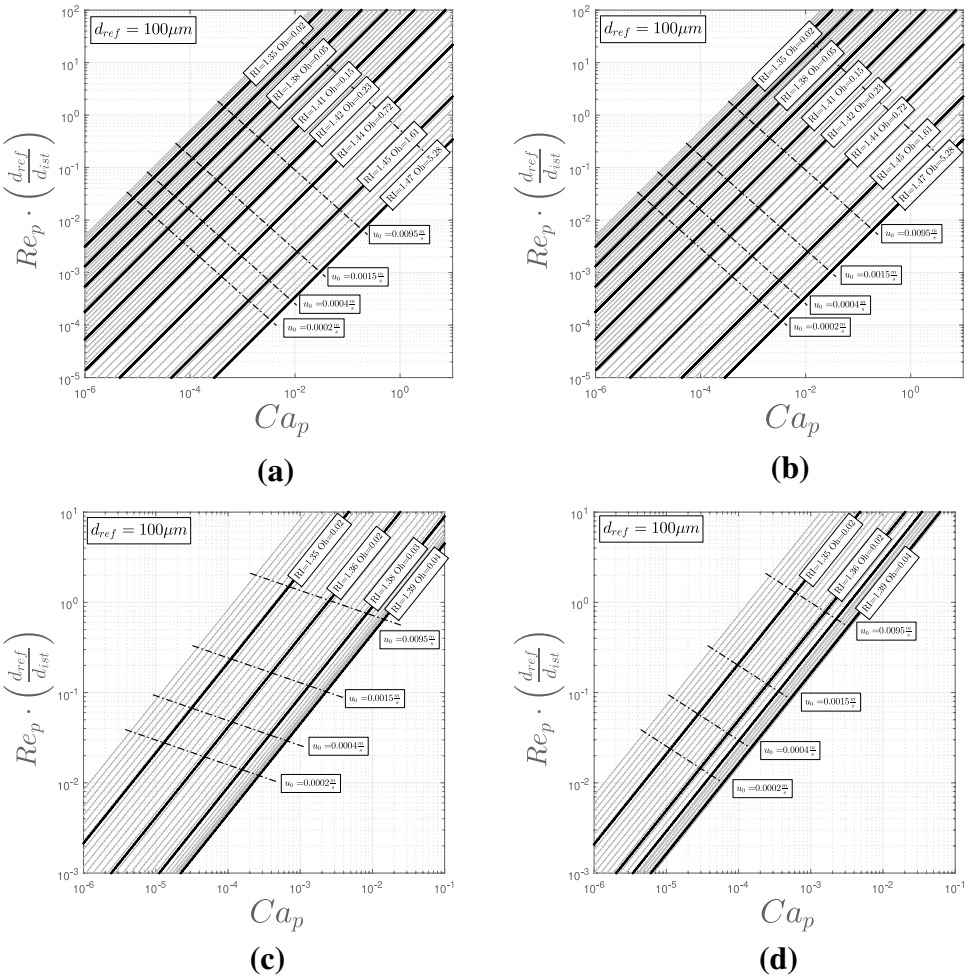

Fig. 10 Nomograms for reachable Ca and Re numbers for a polar continuous phase. **a** Water/glycerol–*n*-hexane/anisole, **b** water/glycerol–*n*-hexane/sunflower-oil, **c** water/DMSO-*n*-hexane/anisole, **d** water/DMSO–*n*-hexane/sunflower-oil

Nomograms for mass-fraction determination

In addition to the MATLAB-script also the relevant properties are provided with this supplementary material, where they can be retrieved from nomograms (Figs. 10, 11). The desired Ca and Re are chosen on the according axis and the corresponding matched Oh and RI of both phases, as well as the superficial velocity, can be received. The RI determines the mass fractions of both phases ξ (Fig. 4) and the associated viscosity ratio (Fig. 6). Via the continuous phase viscosity (Fig. 5) and λ the disperse phase viscosity can be determined. Generally, the systems with a high viscous continuous phase (Fig. 10a, b) cover a larger range of possible Ca and Re, while for the lower viscous continuous phase the parameter range is smaller.

2D-projection of interfacial tension measurements

Regarding the correlations of the interfacial tensions of the double-binary mixture of the refractive index-matched mass-fractions, the 3D visualization of Fig. 7 complicates the assessment. We provide 2D projections of the correlations for the refractive index matched mass-fractions in the following (Fig. 11).

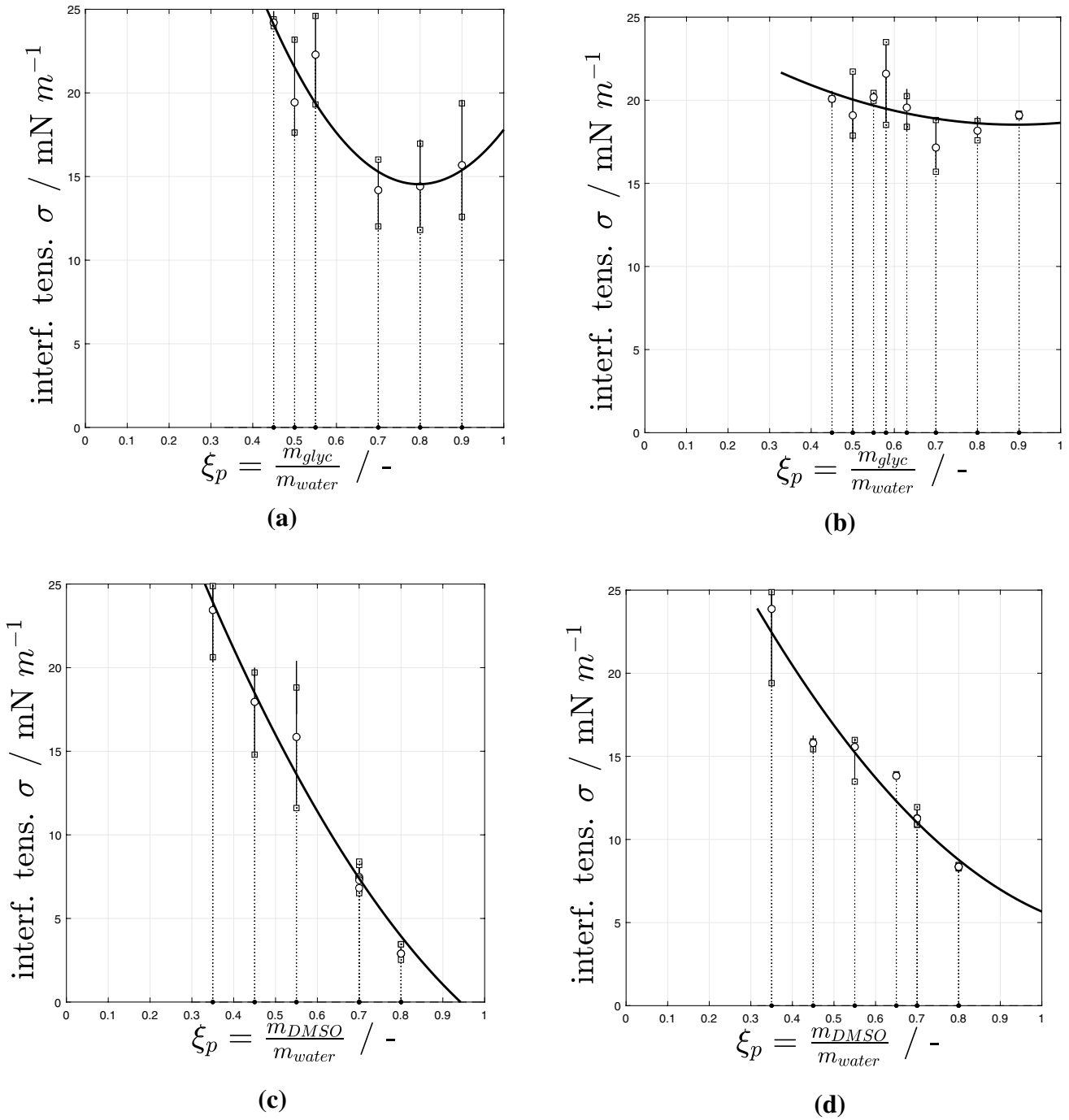

Fig. 11 Correlations of the interfacial tension of the different RI-matched double-binary mixtures in 2D projection. **a** water/glycerol–*n*-hexane/anisole, **b** water/glycerol–*n*-hexane/sunflower-oil, **c** water/DMSO–*n*-hexane/anisole, **d** water/DMSO–*n*-hexane/sunflower-oil

References

Ahmed I, Akram Z, Bule M, Iqbal H (2018) Advancements and potential applications of microfluidic approaches–a review. Chemosensors 6(4):46. https://doi.org/10.3390/chemosensors6040046

Al-Jimaz AS, Al-Kandary JA, Abdul-latif AHM, Al-Zanki AM (2005) Physical properties of anisole+n-alkanes at temperatures between (293.15 and 303.15) k. J Chem Thermodyn 37(7):631–642. https://doi.org/10.1016/j.jct.2004.09.021

Araújo J, Miranda JM, Pinto A, Campos J (2012) Wide-ranging survey on the laminar flow of individual taylor bubbles rising through stagnant newtonian liquids. Int J Multiph Flow 43:131–148. https://doi.org/10.1016/j.ijmultiphaseflow.2012.03.007

Brindise MC, Busse MM, Vlachos PP (2018) Density- and viscosity-matched newtonian and non-newtonian blood-analog solutions

with pdms refractive index. Exp Fluids 59(11):38. https://doi.org/10.1007/s00348-018-2629-6
Budwig R (1994) Refractive index matching methods for liquid flow investigations. Exp Fluids 17(5):350–355. https://doi.org/10.1007/BF01874416
Cadillon J, Saksena R, Pearlstein AJ (2016) Transparent, immiscible, surrogate liquids with matchable refractive indexes: Increased range of density and viscosity ratios. Phys Fluids 28(12):127,102. https://doi.org/10.1063/1.4968512
Chen Y, Li P, Huang PH, Xie Y, Mai JD, Wang L, Nguyen NT, Huang TJ (2014) Rare cell isolation and analysis in microfluidics. Lab Chip 14(4):626–645. https://doi.org/10.1039/c3lc90136j
Chou WL, Lee PY, Yang CL, Huang WY, Lin YS (2015) Recent advances in applications of droplet microfluidics. Micromachines 6(9):1249–1271. https://doi.org/10.3390/mi6091249
Clausell-Tormos J, Lieber D, Baret JC, El-Harrak A, Miller OJ, Frenz L, Blouwolff J, Humphry KJ, Köster S, Duan H, Holtze C, Weitz DA, Griffiths AD, Merten CA (2008) Droplet-based microfluidic platforms for the encapsulation and screening of mammalian cells and multicellular organisms. Chem Biol 15(5):427–437. https://doi.org/10.1016/j.chembiol.2008.04.004, http://www.sciencedirect.com/science/article/pii/S1074552108001506
Clément SA, Guillemain A, McCleney AB, Bardet PM (2018) Options for refractive index and viscosity matching to study variable density flows. Exp Fluids 59(2):434. https://doi.org/10.1007/s00348-018-2496-1
Ern P, Risso F, Fabre D, Magnaudet J (2012) Wake-induced oscillatory paths of bodies freely rising or falling in fluids. Annu Rev Fluid Mech 44(1):97–121. https://doi.org/10.1146/annurev-fluid-120710-101250
González C, Resa JM, Ruiz A, Gutiérrez JI (1996) Densities of mixtures containing n-alkanes with sunflower seed oil at different temperatures. J Chem Eng Data 41(4):796–798. https://doi.org/10.1021/je960053p
Helmers T, Kemper P, Thöming J, Mießner U (2019) Determining the flow-related cap deformation of taylor droplets at low ca numbers using ensemble-averaged high-speed images. Exp Fluids 60(7):66. https://doi.org/10.1007/s00348-019-2757-7
Hosokawa M, Nishikawa Y, Kogawa M, Takeyama H (2017) Massively parallel whole genome amplification for single-cell sequencing using droplet microfluidics. Sci Rep 7(1):5199. https://doi.org/10.1038/s41598-017-05436-4
Kang DK, Ali MM, Zhang K, SHuang S, Peterson E, Digman MA, Gratton E, Zhao W (2014) Rapid detection of single bacteria in unprocessed blood using integrated comprehensive droplet digital detection. Nat Commun 5:5427. https://doi.org/10.1038/ncomms6427
Khodaparast S, Borhani N, Tagliabue G, Thome JR (2013) A micro particle shadow velocimetry (μpsv) technique to measure flows in microchannels. Exp Fluids 54(2):1474. https://doi.org/10.1007/s00348-013-1474-x
Kinoshita H, Kaneda S, Fujii T, Oshima M (2007) Three-dimensional measurement and visualization of internal flow of a moving droplet using confocal micro-piv. Lab Chip 7:338–346. https://doi.org/10.1039/B617391H
Kobayashi J, Mori Y, Kobayashi S (2006) Multiphase organic synthesis in microchannel reactors. Chem Asian J 1(1–2):22–35. https://doi.org/10.1002/asia.200600058
Kovalev AV, Yagodnitsyna AA, Bilsky AV (2018) Flow hydrodynamics of immiscible liquids with low viscosity ratio in a rectangular microchannel with t-junction. Chem Eng J 352:120–132. https://doi.org/10.1016/j.cej.2018.07.013
Kralj JG, Sahoo HR, Jensen KF (2007) Integrated continuous microfluidic liquid-liquid extraction. Lab Chip 7(2):256–263. https://doi.org/10.1039/b610888a
Krohn B, Manera A, Petrov V (2018) A novel method to create high density stratification with matching refractive index for optical flow investigations. Exp Fluids 59(4):434. https://doi.org/10.1007/s00348-018-2522-3
Lang P, Hill M, Krossing I, Woias P (2012) Multiphase minireactor system for direct fluorination of ethylene carbonate. Chem Eng J 179:330–337. https://doi.org/10.1016/j.cej.2011.11.015, http://www.sciencedirect.com/science/article/pii/S1385894711013945
LeBel RG, Goring DAI (1962) Density, viscosity, refractive index, and hygroscopicity of mixtures of water and dimethyl sulfoxide. Journal of Chemical and Engineering Data
Liu Z, Zhang L, Pang Y, Wang X, Li M (2017) Micro-piv investigation of the internal flow transitions inside droplets traveling in a rectangular microchannel. Microfluid Nanofluid 21(12):180. https://doi.org/10.1007/s10404-017-2019-z
Ma S, Sherwood JM, Huck WTS, Balabani S (2014) On the flow topology inside droplets moving in rectangular microchannels. Lab Chip 14(18):3611–3620. https://doi.org/10.1039/c4lc00671b
Magnaudet J, Eames I (2000) The motion of high-reynolds-number bubbles in inhomogeneous flows. Annu Rev Fluid Mech 32(1):659–708. https://doi.org/10.1146/annurev.fluid.32.1.659
Mazutis L, Gilbert J, Ung WL, Griffiths AD, Heyman JA (2013) Single-cell analysis and sorting using droplet-based microfluidics. Nat Protoc 8:870–891. https://doi.org/10.1038/nprot.2013.046
Miessner U, Lindken R, Westerweel J (2008) Velocity measurements in microscopic two-phase flows by means of micro piv. In: Proceedings of the 6th International Conference on Nanochannels, Microchannels and Minichannels—2008, ASME, New York, NY, pp 1111–1118. https://doi.org/10.1115/ICNMM2008-62093
Najjari MR, Hinke JA, Bulusu KV, Plesniak MW (2016) On the rheology of refractive-index-matched, non-newtonian blood-analog fluids for piv experiments. Exp Fluids 57(6):1704. https://doi.org/10.1007/s00348-016-2185-x
Park JS, Kihm KD (2006) Three-dimensional micro-ptv using deconvolution microscopy. Exp Fluids 40(3):491–499. https://doi.org/10.1007/s00348-005-0090-9
Piao Y, Han DJ, Azad MR, Park M, Seo TS (2015) Enzyme incorporated microfluidic device for in-situ glucose detection in water-in-air microdroplets. Biosens Bioelectron 65:220–225. https://doi.org/10.1016/j.bios.2014.10.032
Rao SS, Wong H (2018) The motion of long drops in rectangular microchannels at low capillary numbers. J Fluid Mech 852:60–104. https://doi.org/10.1017/jfm.2018.521
Rocha Luis A M, Miranda JM, Campos JBLM (2017) Wide range simulation study of taylor bubbles in circular milli and microchannels. Micromachines 8(5):154. https://doi.org/10.3390/mi8050154
Saksena R, Christensen KT, Pearlstein AJ (2015) Surrogate immiscible liquid pairs with refractive indexes matchable over a wide range of density and viscosity ratios. Phys Fluids 27(8):087,103. https://doi.org/10.1063/1.4928030
Shi H, Nie K, Dong B, Long M, Xu H, Liu Z (2019) Recent progress of microfluidic reactors for biomedical applications. Chem Eng J 361:635–650. https://doi.org/10.1016/j.cej.2018.12.104
Sinzato YZ, Sousa Dias NJ, Cunha FR (2017) An experimental investigation of the interfacial tension between liquid-liquid mixtures in the presence of surfactants. Exp Thermal Fluid Sci 85:370–378. https://doi.org/10.1016/j.expthermflusci.2017.03.011
Song H, Chen DL, Ismagilov RF (2006) Reactions in droplets in microfluidic channels. Angewandte Chemie International Edition 45(44):7336–7356. https://doi.org/10.1002/anie.200601554, https://onlinelibrary.wiley.com/doi/abs/10.1002/anie.200601554
Tanimu A, Jaenicke S, Alhooshani K (2017) Heterogeneous catalysis in continuous flow microreactors: a review of methods and applications. Chem Eng J 327:792–821. https://doi.org/10.1016/j.cej.2017.06.161

Weast RC (ed) (1989) CRC handbook of chemistry and physics: a ready-reference book of chemical and physical data, 70th edn. CRC Press, Boca Raton

Wilkinson M (1972) Extended use of, and comments on, the drop-weight (drop-volume) technique for the determination of surface and interfacial tensions. J Colloid Interface Sci 40(1):14–26. https://doi.org/10.1016/0021-9797(72)90169-5

Wolf A, Hartmann T, Bertolini M, Schemberg J, Grodrian A, Lemke K, Förster T, Kessler E, Hänschke F, Mertens F, Paus R, Lerchner J (2015) Toward high-throughput chip calorimetry by use of segmented-flow technology. Thermochim Acta 603:172–183. https://doi.org/10.1016/j.tca.2014.10.021 chip Calorimetry

Wright SF, Zadrazil I, Markides CN (2017) A review of solid-fluid selection options for optical-based measurements in single-phase liquid, two-phase liquid-liquid and multiphase solid-liquid flows. Exp Fluids 58(9):357. https://doi.org/10.1007/s00348-017-2386-y

Zhao CX, Middelberg AP (2011) Two-phase microfluidic flows. Chem Eng Sci 66(7):1394–1411. https://doi.org/10.1016/j.ces.2010.08.038

Affiliations

Thorben Helmers[1] · Philip Kemper[2] · Ulrich Mießner[1] · Jorg Thöming[2]

Philip Kemper
pkemper@uni-bremen.de

Ulrich Mießner
miessner@uvt.uni-bremen.de

Jorg Thöming
thoeming@uni-bremen.de

[1] Department of Environmental Process Engineering, University of Bremen, Leobener Str. 6, 28359 Bremen, Germany

[2] Department of Chemical Process Engineering, University of Bremen, Leobener Str. 6, 28359 Bremen, Germany